



Structural, Infrared, Magnetic, and Electrical Properties of $\text{Ni}_{0.6}\text{Cd}_{0.2}\text{Cu}_{0.2}\text{Fe}_2\text{O}_4$ Ferrites Synthesized Using Sol-Gel Method Under Different Sintering Temperatures

Noura Kouki^{1,2} · Sobhi Hcini³ · Reema Aldawas¹ · Michel Boudard⁴

Received: 5 October 2018 / Accepted: 19 November 2018 / Published online: 6 December 2018
© Springer Science+Business Media, LLC, part of Springer Nature 2018

Abstract

$\text{Ni}_{0.6}\text{Cd}_{0.2}\text{Cu}_{0.2}\text{Fe}_2\text{O}_4$ ferrites were synthesized using sol-gel method under different sintering temperatures. XRD patterns with the Rietveld refinement indicate that samples crystallize in the cubic spinel structure. The increase of sintering temperature leads successively to the increase of lattice constant, average crystallite size, intensities of absorption bands, magnetization, and electrical conductivity of the prepared ferrites. Dielectric constants decrease with frequency and their behaviors have been investigated using the interfacial polarization theory predicted by Maxwell. The modulus analysis shows the presence of electrical relaxation phenomenon and non-Debye nature for the samples. An appropriate electrical equivalent circuit was used to analyze the Nyquist plots, and the results show that the conduction mechanism of the synthesized ferrites is mainly due to the grain boundary contribution.

Keywords Ferrites · Sol-gel method · Rietveld refinement · Infrared properties, conductivity · Dielectric properties

1 Introduction

Spinel ferrites with general formula AB_2O_4 (where A and B are the metal cations present at tetrahedral and octahedral positions, respectively) are widely used in electronic applications such as gas sensors, information storage systems, computer memory chips, microwave devices, magnetic recording media, transducers, transformers, and other devices [1]. These

numerous applications are due to the fact that these materials have excellent properties such as high initial permeability, high saturation magnetization, high resistivity, and low magnetic losses [2]. Research which has been conducted on ferrite materials showed that many parameters could affect their properties. For example, it has been revealed that the anomalous properties (i.e., microstructural, electrical, magnetic) of ferrites depend on the sintering temperature (ST) values. In this context, many studies have been presented in the literature. Reddy et al. reported the effect of ST on structural and magnetic properties of NiCuZn and MgCuZn ferrites [3]. The same study was investigated by Patil et al. for lithium chromium ferrite [4]. Kannan et al. studied the structural, magnetic, and optical properties of $\text{Ni}_{0.5}\text{Zn}_{0.5}\text{Fe}_2\text{O}_4$ ferrite nanoparticles at different ST [5]. Furthermore, the effect of ST of structural and magnetic properties of nanostructured $\text{Ni}_{0.3}\text{Zn}_{0.7}\text{Fe}_2\text{O}_4$ ferrite was examined by Rahimi et al. [6].

Along this line, we prepared in this work ferrite samples with $\text{Ni}_{0.6}\text{Cd}_{0.2}\text{Cu}_{0.2}\text{Fe}_2\text{O}_4$ compositions using sol-gel method under different ST (900 °C, 1000 °C, 1100 °C, and 1200 °C). After that, their microstructural, infrared, magnetic, and impedance spectroscopic properties are successively investigated at room temperature (RT).

✉ Sobhi Hcini
hassini271185@gmail.com

¹ Department of Chemistry, College of Science and Arts, Qassim University, Buraydah, Saudi Arabia

² Laboratory of Water, Technopole of Borj Cedria (CERTE), Membranes and Environment Biotechnology (EMBE), 2050 Hammam Lif, Tunisia

³ Research Unit of Valorization and Optimization of Exploitation of Resources, Faculty of Science and Technology of Sidi Bouzid, University of Kairouan, University Campus Agricultural City, 9100 Sidi Bouzid, Tunisia

⁴ LMGP, CNRS, University of Grenoble Alpes, 38000 Grenoble, France

2 Experimental Details

The sol-gel method was used to prepare $\text{Ni}_{0.6}\text{Cd}_{0.2}\text{Cu}_{0.2}\text{Fe}_2\text{O}_4$ ferrites by using $\text{Ni}(\text{NO}_3)_2 \cdot 6\text{H}_2\text{O}$, $\text{Cd}(\text{NO}_3)_2 \cdot 4\text{H}_2\text{O}$, $\text{Cu}(\text{NO}_3)_2 \cdot 4\text{H}_2\text{O}$, and $\text{Fe}(\text{NO}_3)_3 \cdot 9\text{H}_2\text{O}$ nitrates. Figure 1 shows the different synthesis steps of the samples. The free surface morphologies of samples in pellets form were analyzed by scanning electron microscopy (SEM) using Philips XL30 microscope under an accelerating voltage of 15 kV. X-ray diffractometer (Panalytical X'Pert Pro) using Ni-filtered CuK_α radiation ($\lambda = 1.5406 \text{ \AA}$) was used to record the X-ray diffraction pattern analysis in $20^\circ \leq 2\theta \leq 80^\circ$ angular range. The Rietveld analysis [7] using FullProf software was adopted for detailed structural parameter. FTIR spectra were performed in $400\text{--}1000 \text{ cm}^{-1}$ wavenumber range with resolution of 1 cm^{-1} using Shimadzu Fourier Transform Infrared Spectrophotometer (FTIR-8400S). Hysteresis loops were obtained using vibrating sample magnetometer (VSM) in a maximum applied field of 10 kOe. The frequency dependences of dielectric measurements were evaluated at RT using N4L-NumetriQ (model PSM1735) connected to a computer over $100 \text{ Hz--}1 \text{ MHz}$ frequency range.

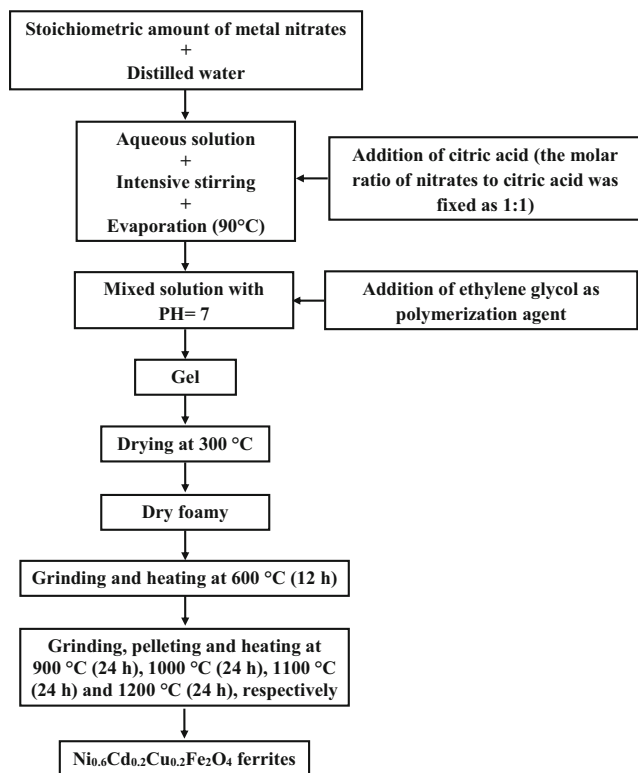


Fig. 1 Synthesis steps by the sol-gel method of $\text{Ni}_{0.6}\text{Cd}_{0.2}\text{Cu}_{0.2}\text{Fe}_2\text{O}_4$ ferrites sintering at different temperatures

3 Results and Discussions

3.1 Microstructural Properties

Figure 2 shows the SEM micrographs for $\text{Ni}_{0.6}\text{Cd}_{0.2}\text{Cu}_{0.2}\text{Fe}_2\text{O}_4$ ferrites sintering at different temperatures. The analysis of these images using ImageJ software shows average particle size of about 0.133, 0.180, 0.211, and $0.412 \mu\text{m}$ for the samples sintered at 900°C , 1000°C , 1100°C , and 1200°C , respectively. Therefore, the SEM images confirm the enlarging of particle size by increasing ST. Indeed, the tendency of particles to join together and constitute large particles with negligible porosity is evidently realized in the sample sintered at 1200°C .

The XRD patterns with the Rietveld refinements of $\text{Ni}_{0.6}\text{Cd}_{0.2}\text{Cu}_{0.2}\text{Fe}_2\text{O}_4$ ferrites at different preparation temperatures varying from 900 to 1200°C are illustrated in Fig. 3. The XRD patterns of all compounds confirm that they belong to the cubic spinel structure. Also, it is observed from the figure that any additional peaks related to impurity phases were detected, confirming the high purity of the prepared samples. The peak indexation was performed using “X’Pert HighScore Plus” software in the cubic $Fd\bar{3}m$ symmetry. In the Rietveld refinement procedure, we proposed the cation distribution $(\text{Cd}_{0.2}^{2+}\text{Fe}_{0.4}^{3+})_A[\text{Ni}_{0.6}^{2+}\text{Cu}_{0.2}^{2+}\text{Fe}_{1.6}^{3+}]_B\text{O}_4^{2-}$, where the brackets () and [] contain the cations occupying the A and B sites, respectively. According to this distribution, the Cd^{2+} ions have preference of occupying the tetrahedral A-sites, whereas the Ni^{2+} and Cu^{2+} ions are known to occupy the octahedral B-sites; and Fe^{3+} ions are distributed on both the sites [8–11]. The crystalline structure of samples has been refined in $Fd\bar{3}m$ symmetry with atomic positions taken at $8a (1/8, 1/8, 1/8)$ for $(\text{Cd}_{0.2}^{2+}\text{Fe}_{0.4}^{3+})_A$ cations, $16d (1/2, 1/2, 1/2)$ for $[\text{Ni}_{0.6}^{2+}\text{Cu}_{0.2}^{2+}\text{Fe}_{1.6}^{3+}]_B$ cations, and $32e (x, y, z)$ for O. A good agreement between the observed and calculated profiles was noticed in Fig. 3. The refined structural parameters are listed in Table 1 for all samples. The goodness of fit (χ^2) shows small values of residual indicating excellent agreement between observed and calculated XRD data. With increasing ST, it is remarkable that both lattice constant (a) and unit cell volume (V) increase, in accordance with the results found in previous works [4, 6]. Also, the obtained oxygen coordinate values are characteristic of the spinel-type structure [12, 13]. The X-ray density was calculated according to the following equation [14]:

$$d_x = \frac{8M}{Na^3} \quad (1)$$

where M is the molecular weight of the sample, N is the Avogadro’s number, and a is the lattice constant. The estimated d_x values decrease as the ST increases (see Table 1). The average crystallite size was estimated from XRD peaks using the Scherer formula as [15]:

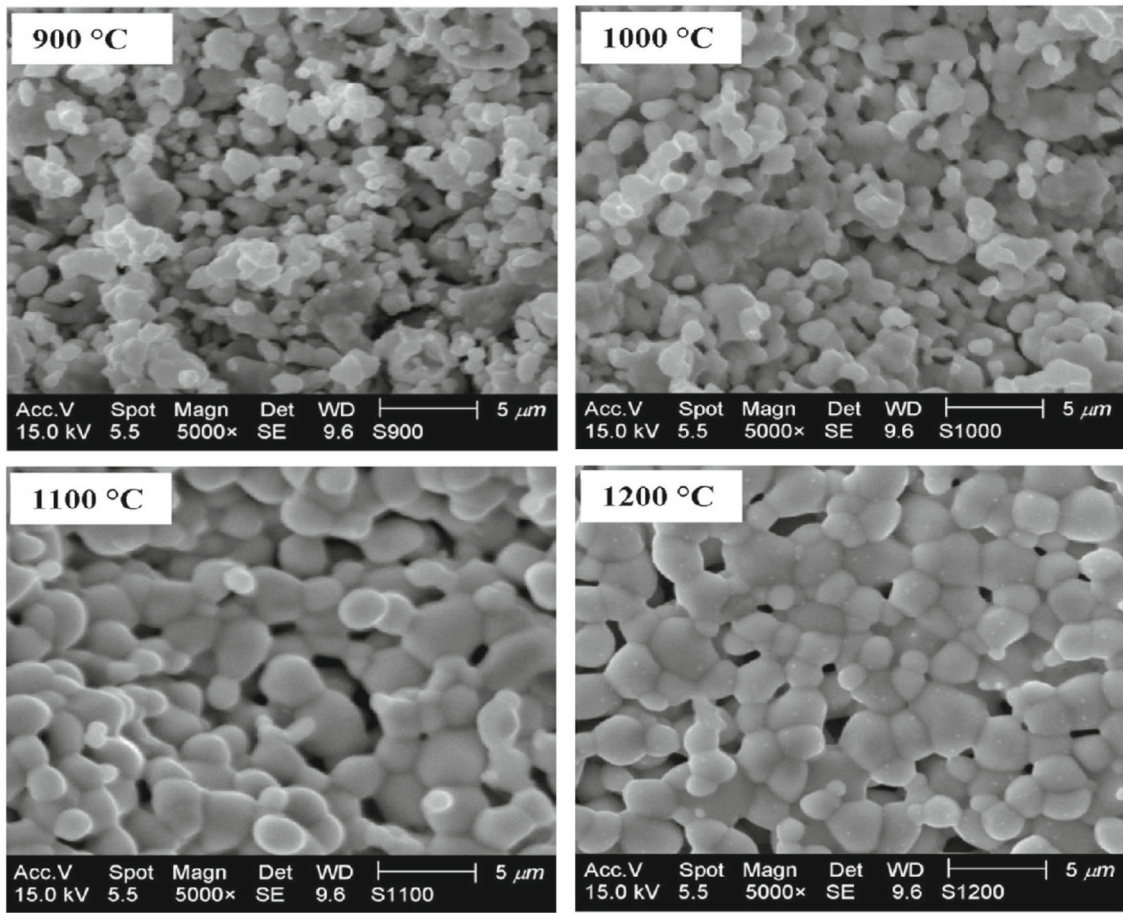


Fig. 2 Scanning electron micrographs for Ni_{0.6}Cd_{0.2}Cu_{0.2}Fe₂O₄ ferrites sintering at different temperatures

$$D = \frac{0.9 \lambda}{\beta \cos(\theta)} \tag{2}$$

where λ is the wavelength of X-ray, β is the corrected full-width half maxima of the XRD peaks, and θ is the Bragg angle. The D values presented in Table 1 increase with ST in good agreement with other similar results [4, 6]. The results are consistent with SEM observations; however, it is obvious that the crystallite sizes estimated from XRD peaks are smaller than the particle sizes obtained from SEM micrographs. This difference is due to the fact that the particles are composed of several crystallites, due to internal strains or defects in the structure [16].

3.2 Infrared Properties

Generally, in FTIR spectra of spinel ferrites, there are two main characteristic absorption peaks, which are related to the intrinsic vibrations of oxygen bonds with metal cations at A and B sites [17]. To detect these absorption bands, the FTIR spectra of Ni_{0.6}Cd_{0.2}Cu_{0.2}Fe₂O₄ ferrites were carried out at RT and presented in Fig. 4. The obtained spectra confirm well the presence of the two characteristic peaks of spinel ferrites. The first band observed at the frequency (ν_1) in the range of 415–420 cm⁻¹

corresponds to the stretching vibrations of metal-oxygen at the octahedral site. While the second band observed at the frequency (ν_2) in the range of 535–544 cm⁻¹ is attributed to the vibration of metal-oxygen at the tetrahedral site. The peak positions corresponding to ν_1 and ν_2 frequencies are listed in Table 2 and shown in Fig. 4 for all samples. It is clear from this table that the values of ν_1 and ν_2 frequencies appear to increase with increasing ST. In the other hand, the difference between the band positions is related to the difference in the metal-oxygen bond distances for tetrahedral and octahedral sites (see Table 1) due to temperature effect [18]. The force constants (K_T) and (K_O) for the tetrahedral and octahedral sites, respectively, are calculated according to the following relation [19, 20]:

$$K_{T/O} = 4\pi^2 c^2 \nu^2 m \tag{3}$$

where c is the light speed, ν is the vibration frequency for tetrahedral and octahedral sites, and m is the reduced mass of the Fe³⁺ and O²⁻ ions. The results presented in Table 3 show a trend increase of both K_T and K_O values with ST. This behavior can be attributed to the decrease of R_A and R_B bond lengths of cation-oxygen in A and B sites (see Fig. 5). Since the R_A and R_B bond lengths decrease with the increase of ST, the energy required to break short bonds is high, and this supports an increase in the

Fig. 3 The Rietveld analysis of XRD patterns of $\text{Ni}_{0.6}\text{Cd}_{0.2}\text{Cu}_{0.2}\text{Fe}_2\text{O}_4$ ferrites sintering at different temperatures. The bottom line (blue) represents the difference between the XRD data (red) and calculated fit (black), and the green lines are the Bragg positions

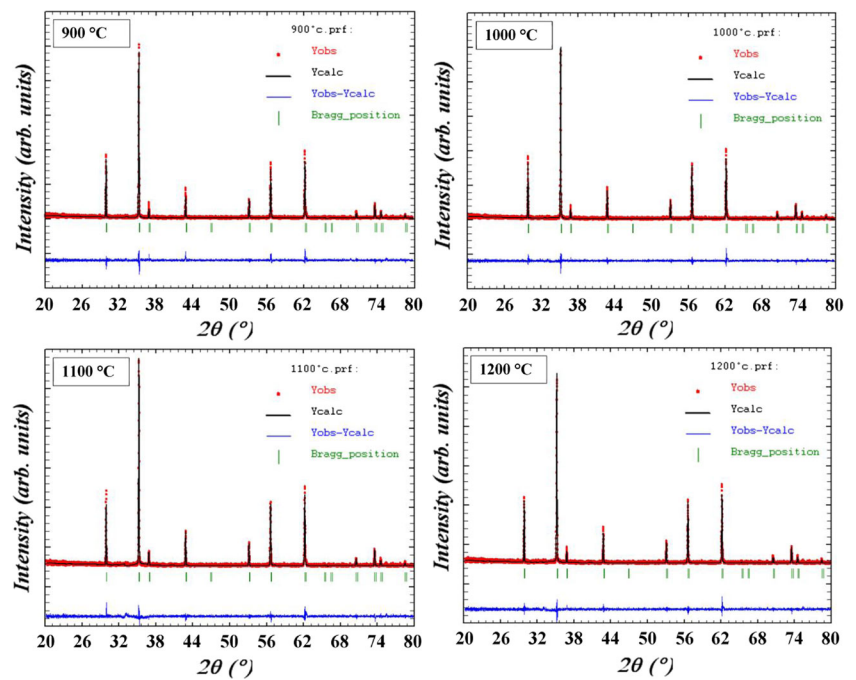


Table 1 RT structural parameters obtained from Rietveld refinement for $\text{Ni}_{0.6}\text{Cd}_{0.2}\text{Cu}_{0.2}\text{Fe}_2\text{O}_4$ ferrites sintering at different temperatures. The numbers in parentheses are estimated standard deviations to the last significant digit. *WP* Wyckoff positions, *SS* site symmetry, *AP* atomic

positions, *OP* occupancy factors, *B_{iso}* isotropic Debye-Waller factor, *R_A* and *R_B* cation-oxygen distances in A and B sites, *d_x* X-ray density, *D* average crystallite sizes estimated from XRD peaks. Agreement factors of profile *R_p*, weighted profile *R_{wp}*, and structure *R_f*; χ^2 the goodness of fit

ST			900 °C	1000 °C	1100 °C	1200 °C
Space group			Fd-3m	Fd-3m	Fd-3m	Fd-3m
Cell parameters	<i>a</i> (Å)		8.4362 (2)	8.4382 (3)	8.4403 (2)	8.4421 (2)
	<i>V</i> (Å ³)		600.41 (2)	600.83 (3)	601.29 (2)	601.67 (2)
Atoms	Cd/Fe ₁	<i>WP</i>	4c	4c	4c	4c
		<i>SS</i>	−43m	−43m	−43m	−43m
		<i>AP</i>	<i>x</i> = <i>y</i> = <i>z</i>	<i>x</i> = <i>y</i> = <i>z</i>	<i>x</i> = <i>y</i> = <i>z</i>	<i>x</i> = <i>y</i> = <i>z</i>
		<i>B_{iso}</i> (Å ²)	2.34 (1)	0.64 (1)	0.48 (1)	1.10 (1)
	Ni/Cu/Fe ₂	<i>WP</i>	16d	16d	16d	16d
		<i>SS</i>	−3m	−3m	−3m	−3m
		<i>AP</i>	<i>x</i> = <i>y</i> = <i>z</i>	<i>x</i> = <i>y</i> = <i>z</i>	<i>x</i> = <i>y</i> = <i>z</i>	<i>x</i> = <i>y</i> = <i>z</i>
		<i>B_{iso}</i> (Å ²)	0.03 (1)	1.11 (1)	1.78 (1)	1.29 (1)
	O	<i>WP</i>	32e	32e	32e	32e
		<i>SS</i>	3m	3m	3m	3m
		<i>AP</i>	<i>x</i> = <i>y</i> = <i>z</i>	<i>x</i> = <i>y</i> = <i>z</i>	<i>x</i> = <i>y</i> = <i>z</i>	<i>x</i> = <i>y</i> = <i>z</i>
		<i>B_{iso}</i> (Å ²)	1.43 (0)	2.18 (9)	1.80 (0)	1.41 (2)
Structural parameters	<i>R_A</i> (Å)		1.969 (8)	1.963 (8)	1.954 (8)	1.946 (11)
	<i>R_B</i> (Å)		2.045 (11)	2.038 (8)	2.034 (8)	2.030 (8)
	<i>d_x</i> (g/cm ³)		5.4453	5.4415	5.4373	5.4339
	<i>D</i> (nm)		39	45	48	56
Agreement factors	<i>R_p</i> (%)		21.0	20.1	20.7	21.8
	<i>R_{wp}</i> (%)		29.1	29.9	29.9	31.4
	<i>R_f</i> (%)		11.2	10.4	10.3	13.2
	χ^2 (%)		1.27	1.24	1.34	1.47

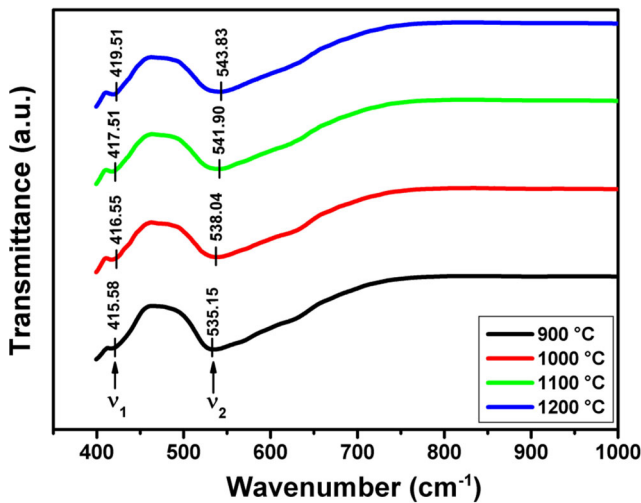


Fig. 4 FTIR spectra at RT of Ni_{0.6}Cd_{0.2}Cu_{0.2}Fe₂O₄ ferrites sintering at different temperatures

force constants of tetrahedral and octahedral sites [21].

3.3 Magnetic Properties

The magnetic hysteresis (M-H) loops obtained at RT at an applied field of ± 10 kOe for Ni_{0.6}Cd_{0.2}Cu_{0.2}Fe₂O₄ ferrites sintering at different temperatures are shown in Fig. 6. The estimated values of saturation magnetization (*M_s*), remanent magnetization (*M_r*), and coercivity (*H_c*) are summarized in Table 2. It is clear that *M_s* values were affected by the increase of ST. This can be attributed to the increase of the average crystallite size of the samples. This is in good agreement with the works reported by other authors [22, 23]. Also the decrease of *H_c* values could be interpreted by taking into consideration the augmentation of the average grain size with ST. In fact, the largest grains have a tendency to consist the greatest number of domain walls. The magnetization/demagnetization provoked by the domain wall movement needs less energy than that needed by domain rotation. The same as the number of walls rises with grain size, the contribution of wall movement to magnetization/demagnetization is superior to that of the domain rotation. Thus, the sample sintered at 1200 °C with bigger grains is predictable to have a low coercivity *H_c* comparing with the sample sintered at 900 °C.

Table 2 Infrared and magnetic parameters at RT for Ni_{0.6}Cd_{0.2}Cu_{0.2}Fe₂O₄ ferrites sintering at different temperatures

ST	ν_1 (cm ⁻¹)	ν_2 (cm ⁻¹)	$K_O \times 10^5$ (dyne cm ⁻¹)	$K_T \times 10^5$ (dyne cm ⁻¹)	<i>M_s</i> (emu g ⁻¹)	<i>M_r</i> (emu g ⁻¹)	<i>H_c</i> (Oe)
900 °C	415.58	535.15	1.578	2.629	42.79	17.56	322.25
1000 °C	416.55	538.04	1.593	2.657	52.79	12.68	226.89
1100 °C	417.51	541.90	1.600	2.696	59.39	7.45	139.06
1200 °C	419.51	543.83	1.615	2.715	68.78	3.58	68.80

3.4 Electrical Properties

3.4.1 Conductivity

In order to study the conduction process of the prepared ferrites, which is in general due to the electron hopping between Fe²⁺ and Fe³⁺ ions occupying the octahedral site, the variation of the electrical conductivity (σ) with frequency at RT is carried out and the results are displayed in Fig. 7. For all samples, it can be seen that the σ values have the same appearance for each ST. In fact, at the beginning, the conductivity remains constant by increasing the frequency until a certain value called hopping frequency ($f_h \approx 10^5$ Hz) which has a displacement towards high frequencies as the ST increases. This constancy could be explained by more activity of the low conductive grain boundaries in this frequency region and therefore Fe²⁺ ↔ Fe³⁺ electron hopping is less. This frequency region corresponds to the *dc* conductivity (σ_{dc}). For $f > f_h$, it is observable that the conductivity increases exponentially with frequency. The conductive grains become more active in this frequency range, which promote the conduction process of the samples. To verify these observations, the conductivity data are modeled using the following Jonscher power law [24]:

$$\sigma_{tot} = \sigma_{dc} + Bf^s \tag{4}$$

where *B* and *s* are the pre-exponential and exponent factors, respectively. The modeling of experimental curves using Eq. (4) shows good agreement between the theoretical and experimental curves of the studied samples (see Fig. 7). The fitting parameters are given in Table 3. It is clear from this table that σ_{dc} and *s* values increase with increasing ST, due to an augmentation of the electron hopping which also rises with temperature. In the other hand, the *s* values are superior to 1 for all temperatures indicating that the electron hopping occurs between neighboring sites, according to the Funke criterion [25].

3.4.2 Dielectric Constants

This part is devoted to the study of dielectric properties of Ni_{0.6}Cd_{0.2}Cu_{0.2}Fe₂O₄ ferrites, sintered at different temperatures. The frequency variations of their real and imaginary

Table 3 Fitting parameters obtained from the experimental data of conductivity as a function of frequency at RT for $\text{Ni}_{0.6}\text{Cd}_{0.2}\text{Cu}_{0.2}\text{Fe}_2\text{O}_4$ ferrites sintering at different temperatures

ST	$\sigma_{dc} \times 10^{-5}$ (S m^{-1})	$B \times 10^{-12}$	s	χ^2
900 °C	0.54	10.23	1.075	0.996
1000 °C	1	2.380	1.2301	0.995
1100 °C	3	0.867	1.308	0.997
1200 °C	5	0.089	1.475	0.995

parts of permittivity as well as their loss factors at RT are presented in Fig. 8a–c. For all samples, it should be noted that the values of ε' , ε'' , and $\tan\delta$ are high in the low-frequency region. Then, the values of these dielectric constants decrease monotonically and become very low in the high-frequency region. Similar results have been observed in other studies [26, 27], and in most cases, the authors have interpreted the behavior of these dielectric constants by the theory of interfacial polarization predicted by Maxwell [28]. Indeed, the dielectric structure of spinel ferrites is generally divided into two parts: grains that have high conductivity and grain boundaries that act as insulators. Under the application of an electric field, the displacement of the charges in the grains is interrupted at the grain boundaries, which causes an accumulation of the charges at the interface, then the appearance of an interfacial polarization. In fact, electron exchange does not follow the applied field in the high-frequency region, resulting in a decrease in the contribution of interfacial polarization. As a result, the dielectric constant values become very low towards the high frequencies reaching values of the order of 10^{-1} , making the samples promising candidates for the high-frequency applications [29]. In the other hand, the dielectric constant values decrease with increasing ST at low-frequency

Fig. 5 Force constants K_T and K_O versus bond lengths R_A and R_B

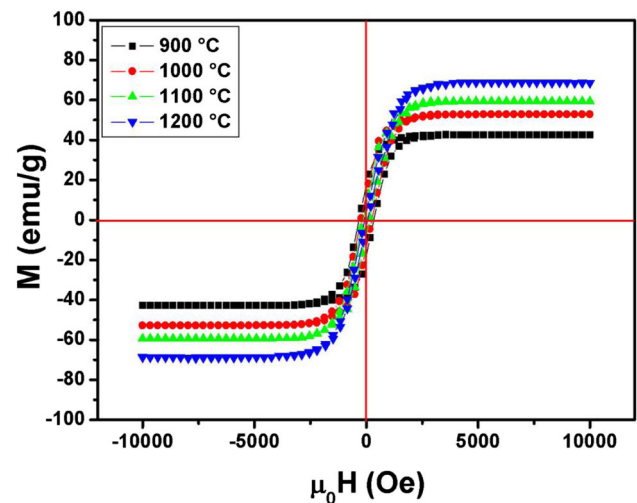
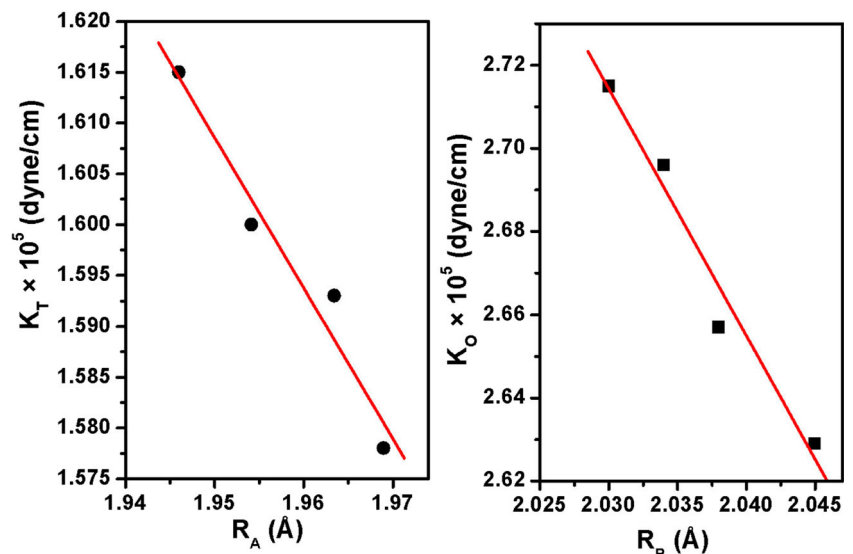


Fig. 6 Magnetic hysteresis curves measured at RT for $\text{Ni}_{0.6}\text{Cd}_{0.2}\text{Cu}_{0.2}\text{Fe}_2\text{O}_4$ ferrites sintering at different temperatures

region, which is in good agreement with the rise of conductivity.

3.4.3 Modulus

The frequency variation of real part of electrical module at RT for $\text{Ni}_{0.6}\text{Cd}_{0.2}\text{Cu}_{0.2}\text{Fe}_2\text{O}_4$ ferrites sintered at different temperatures is illustrated in Fig. 9a. For all the samples, the $M'(f)$ variation can be divided into three parts: (i) at low frequencies ($f < 10^3$ Hz), the M' values are very low, which confirms that the polarization of the electrode makes a negligible contribution to the materials [30]. (ii) At intermediate frequencies (10^3 Hz $< f < 10^6$ Hz), an exponential increase in M' values was observed. (iii) At high frequencies ($f > 10^6$ Hz), the values of M' have a tendency to saturate at a maximum asymptotic value. This may be due to the short-range mobility of charge carriers [31, 32]. Figure 9b shows the $M''(f)$ curves at RT for

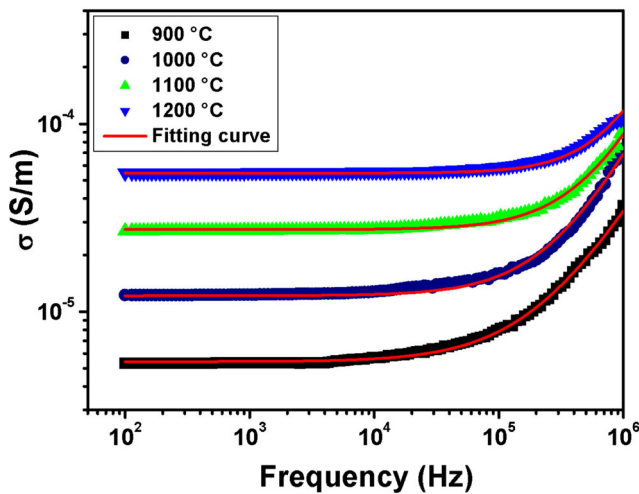


Fig. 7 Variation of conductivity vs. frequency at RT fitted with the Jonscher power law for $\text{Ni}_{0.6}\text{Cd}_{0.2}\text{Cu}_{0.2}\text{Fe}_2\text{O}_4$ ferrites sintering at different temperatures

the prepared samples. Well-resolved peaks are observed from these curves at characteristic frequencies ($f_{M''}^{\text{max}}$). Due to the thermal activation of the charge carriers resulting from the increase of ST, the positions of these peaks move to the higher frequency side. The $M''(f)$ curves have been well adjusted by using the Bergman proposed Kohlrausch, Williams, and Watts (KWW) function [33]:

$$M'' = M''_{\text{max}} / \left[1 - \beta + \left(\frac{\beta}{1 + \beta} \right) \left(\beta \left(\frac{f_{\text{max}}}{f} \right) + \left(\frac{f}{f_{\text{max}}} \right)^\beta \right) \right] \tag{5}$$

where M''_{max} is the peak maxima and f_{max} its corresponding frequency. β is the stretching factor ($0 < \beta < 1$), which decides whether the relaxation in dielectric is Debye or non-Debye in nature [34]. The fitting parameters of $M''(f)$ data using Eq. (5) are given in Table 5. On the one hand, the β values for all samples turned out to be less than unity, showing so a non-Debye nature of the samples, and on the other hand, they increase with increasing ST. This increase is caused by the rise of the average crystallite size with ST which also engenders a significantly drop of the number of dipoles in the grain boundary [35]. Consequently, the interaction between the dipoles in the grain boundaries decreases and, as a result, the relaxation of the dipoles becomes faster. This leads to the increase of the relaxation frequency (f_{max}) and the decrease of the relaxation time, $\tau_{M''} = 1/2\pi f_{\text{max}}$ (see Table 4).

3.4.4 Impedance

Figure 10 depicts the Nyquist plots (Z'' vs. Z') at RT for $\text{Ni}_{0.6}\text{Cd}_{0.2}\text{Cu}_{0.2}\text{Fe}_2\text{O}_4$ ferrites sintered at different temperatures. For each ST, only one semicircle (whose maximum and diameter decrease with increasing ST) is

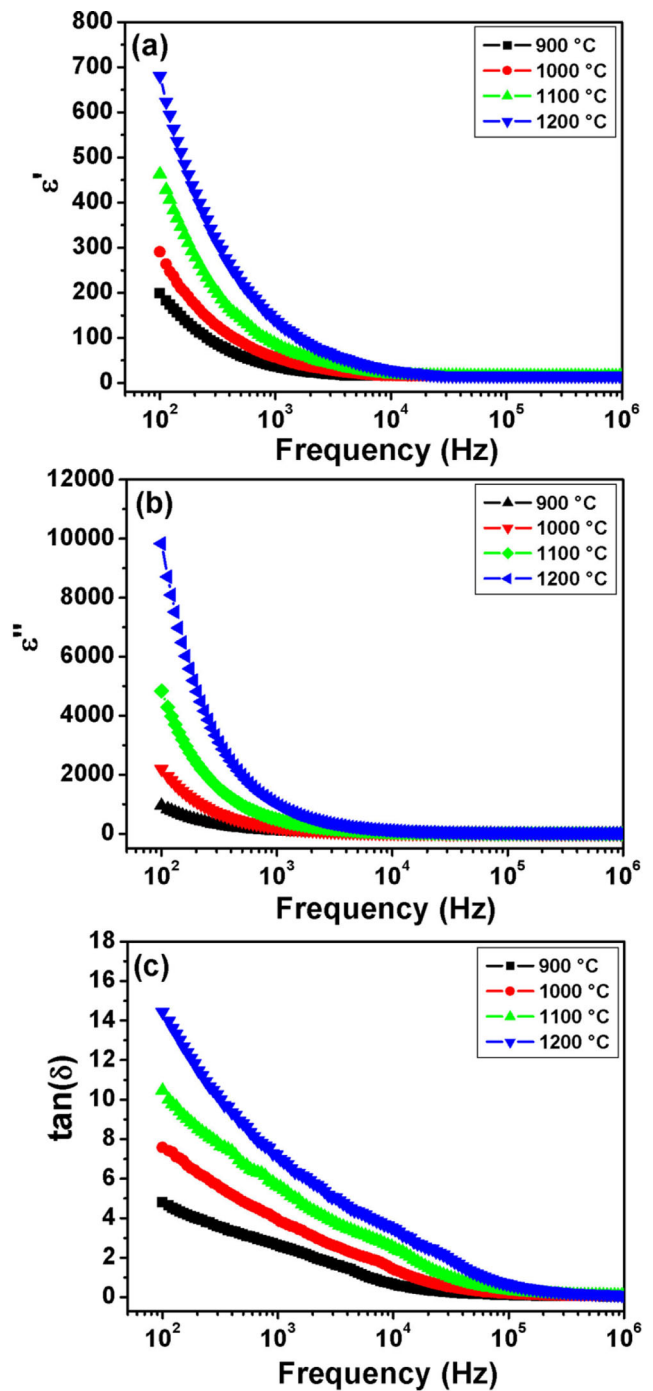


Fig. 8 Frequency dependence at RT of real part of permittivity (a), imaginary part of permittivity (b), and loss factor (c) for $\text{Ni}_{0.6}\text{Cd}_{0.2}\text{Cu}_{0.2}\text{Fe}_2\text{O}_4$ ferrites sintering at different temperatures

observed, indicating just one dominant relaxation phenomenon. In the analysis of impedance data, the Nyquist plots help us to separate the grain and grain-boundary contributions of the samples to the total electrical conductivity over wide frequency range. Indeed, in such plots, the intersection with real axis of the semicircle at low frequencies (right intersect) is ascribed to

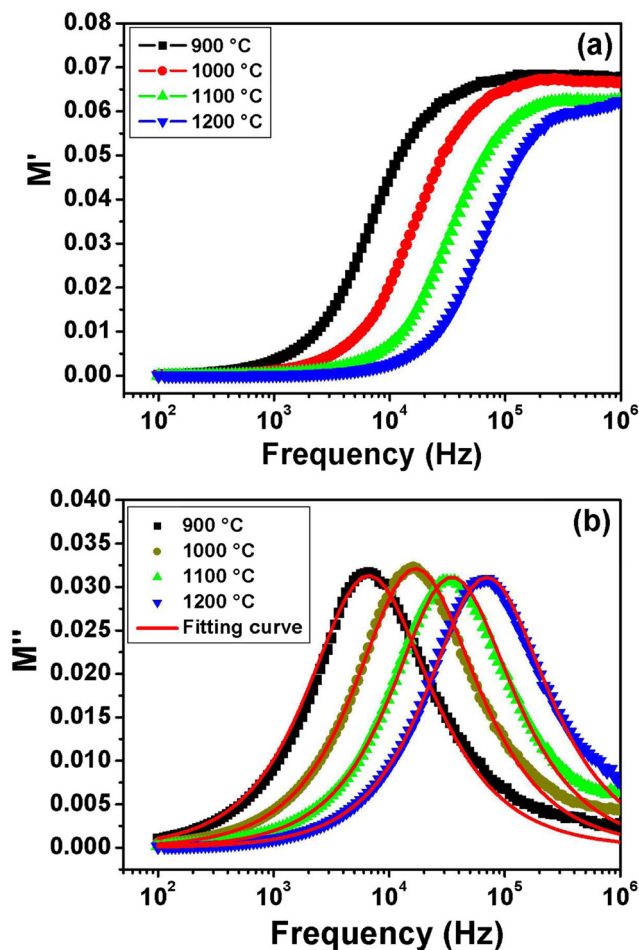


Fig. 9 Frequency dependence at RT of **a** real part (M') and **b** imaginary part (M'') of electrical modulus for $\text{Ni}_{0.6}\text{Cd}_{0.2}\text{Cu}_{0.2}\text{Fe}_2\text{O}_4$ ferrites sintering at different temperatures. Red solid lines represent the fit of experimental data of $M''(f)$ using Eq. (5)

the total resistance (R_T) which is equal to the sum of grain resistance (R_g) and grain boundary resistance (R_{gb}) [36]. On the other hand, the impedance response of grain dominates at high frequencies, so, R_g can be deduced from the left intersect of the semicircle with real axis. As shown in Fig. 10, the left intersections of the semicircles for all samples with the real axis cross the origin. These results suggest that contribution from the grain is not resolved for these samples and their

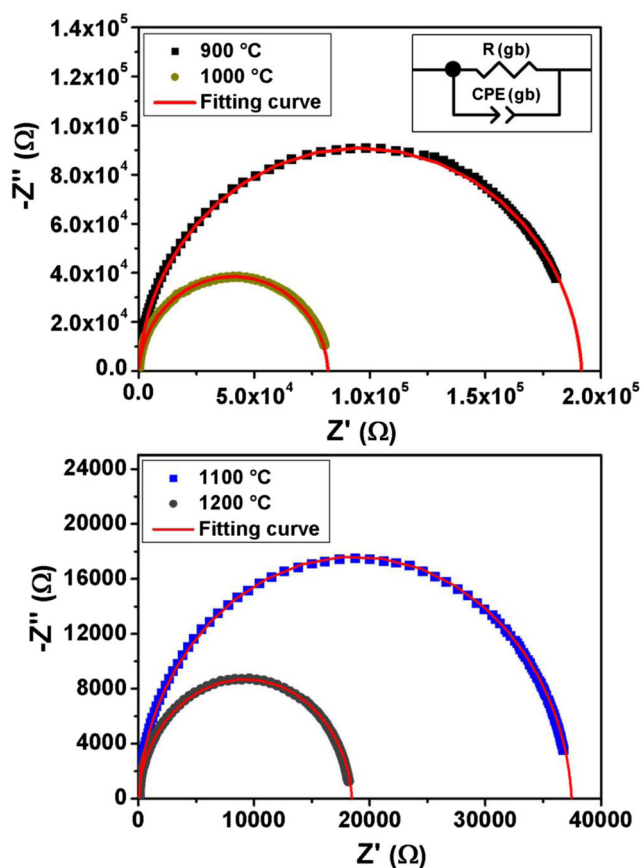


Fig. 10 The Nyquist plots at RT of $\text{Ni}_{0.6}\text{Cd}_{0.2}\text{Cu}_{0.2}\text{Fe}_2\text{O}_4$ ferrites sintering at different temperatures. Inset: the appropriate electrical equivalent circuit used for modeling the impedance spectra

conduction takes place predominantly through the grain boundary [37, 38]. This may be due to a limited frequency range used in this study (100 Hz–1 MHz) or the grain boundary contribution cannot be separated from the grain contribution by the impedance spectroscopy [39]. These interpretations can be more achieved by an adjustment of the Nyquist plots by an appropriate equivalent circuit. As shown in the inset of Fig. 10, the proposed equivalent circuit is of the type of ($R_{gb} // CPE_{gb}$) configuration [37]. Here, R_{gb} represents the grain boundary resistance, while CPE_{gb} is the constant phase element for grain boundaries. The impedance response of a constant phase element (CPE) can be

Table 4 Fitting parameters obtained from the experimental data of imaginary part of electrical modulus as a function of frequency at RT for $\text{Ni}_{0.6}\text{Cd}_{0.2}\text{Cu}_{0.2}\text{Fe}_2\text{O}_4$ ferrites sintering at different temperatures

ST	M'_{\max} ($\times 10^{-4}$)	β	$f_{M'}^{\max}$ (Hz)	τ ($\times 10^{-6}$ s)
900 °C	0.0313	0.917	6662	23.89
1000 °C	0.0321	0.925	16.950	9.389
1100 °C	0.0311	0.932	34.996	4.548
1200 °C	0.0311	0.937	69.975	2.274

Table 5 Electrical parameters of equivalent circuit deduced from the Nyquist plots at RT for $\text{Ni}_{0.6}\text{Cd}_{0.2}\text{Cu}_{0.2}\text{Fe}_2\text{O}_4$ ferrites sintering at different temperatures

ST	R_{gb} (Ω)	$Q \times 10^{-10}$ (F)	α
900 °C	191.680	2.160	0.9666
1000 °C	81.911	2.288	0.9618
1100 °C	37.463	2.447	0.9615
1200 °C	18.471	2.716	0.9614

defined as [40, 41]:

$$Z_{CPE} = \frac{1}{Q(j\omega)^\alpha} \quad (6)$$

where Q is a proportional factor, ω is the angular frequency, and α is an empirical exponent close to 1. The expressions of real (Z') and imaginary (Z'') components of impedance related to the equivalent circuit are given as [42, 43]:

$$Z' = \frac{R_{gb} + \left(1 + R_{gb}Q\omega^\alpha \cos\left(\frac{p\pi}{2}\right)\right)}{\left(1 + R_{gb}Q\omega^\alpha \cos\left(\frac{\alpha\pi}{2}\right)\right)^2 + \left(R_{gb}Q\omega^\alpha \sin\left(\frac{\alpha\pi}{2}\right)\right)^2} \quad (7)$$

$$-Z'' = \frac{R_{gb}^2 Q \omega^\alpha \sin\left(\frac{\alpha\pi}{2}\right)}{\left(1 + R_{gb}Q\omega^\alpha \cos\left(\frac{\alpha\pi}{2}\right)\right)^2 + \left(R_{gb}Q\omega^\alpha \sin\left(\frac{\alpha\pi}{2}\right)\right)^2} \quad (8)$$

The modeling of impedance spectra was performed using Zview software [44]. An excellent agreement between the experimental spectra and the calculated ones was observed (see Fig. 10). The obtained fitted parameters are listed in Table 5. It is clear from this table that R_{gb} values decrease when increasing ST, which indicates an increase of the conductivity. The decrease of grain boundary resistance is due to the fact that the grain boundary effect has assisted in lowering the barrier to the motion of charge carriers paving the way for increased electrical transport with rise in ST [36, 45].

4 Conclusion

$\text{Ni}_{0.6}\text{Cd}_{0.2}\text{Cu}_{0.2}\text{Fe}_2\text{O}_4$ ferrite samples are prepared using sol-gel method at different ST (900 °C, 1000 °C, 1100 °C, and 1200 °C). Their RT microstructural, infrared, magnetic, and impedance spectroscopy properties are successively investigated. The XRD patterns and the Rietveld refinement confirm the cubic spinel-type structure for all samples. Two principal absorption bands are shown from FTIR spectra that are attributed to the stretching vibration of tetrahedral and octahedral sites. The saturation magnetization and conductivity values were also affected by the increase of ST as a consequence of

the gradual increase of average crystallite size. Dielectric constants decrease with frequency due to the decrease in polarization. The variation of electrical modulus shows the presence of an electrical relaxation phenomenon with non-Debye type in the prepared ferrites. From the Nyquist diagram analysis, we found that the resistances of the prepared ferrites resulted mostly from the grain boundary effect.

Funding Information This work was supported by the Deanship of Scientific Research at Al Qassim University under the research Project Number 5090-cosabu-2018-1-14-S.

References

- Meng, Y.Y., Liu, Z.W., Dai, H.C., Yu, Y., Zeng, D.C., Shukla, S., et al.: Powder Technol. **229**, 270 (2012)
- Kolekar, Y.D., Sanchez, L., Rubio, R.E., et al.: Solid State Commun. **184**, 34 (2014)
- Reddy, M.P., Madhuri, W., Ramana, M.V., Reddy, N.R., Kumar, K.V.S., Murthy, V.R.K., Kumar, K.S., Reddy, R.R.: J. Magn. Magn. Mater. **322**, 2819 (2010)
- Patil, R.P., Hankare, P.P., Garadkar, K.M., Sasikala, R.: J. Alloys Compd. **523**, 66 (2012)
- Kannan, Y.B., Saravanan, R., Srinivasan, N., Ismail, I.: J. Magn. Magn. Mater. **423**, 217 (2017)
- Rahimi, M., Kameli, P., Ranjbar, M., Salamati, H.: J. Nanopart. Res. **15**, 1865 (2013)
- Rietveld, H.M.: J. Appl. Crystallogr. **2**, 65 (1969)
- Hakim, M.A., Nath, S.K., Sikder, S.S., Maria, K.H.: J. Phys. Chem. Solids. **74**, 1316 (2013)
- Lohar, K.S., Patange, S.M., Mane, M.L., Shirsath, S.E.: J. Mol. Struct. **1032**, 105 (2013)
- Houshiar, M., Jamilpanah, L.: Mater. Res. Bull. **98**, 213 (2018)
- Gholizadeh, A., Jafari, E.: J. Magn. Magn. Mater. **422**, 328 (2017)
- Pailhé, N., Wattiaux, A., Gaudon, M., Demourgues, A.: J. Solid State Chem. **181**, 1040 (2008)
- Verma, K., Kumar, A., Varshney, D.: J. Alloys Compd. **526**, 91 (2012)
- Anwar, M.S., Ahmed, F., Koo, B.H.: Acta Mater. **71**, 100–107 (2014)
- Ahmed, M.A., Afify, H.H., El Zawawia, I.K., Azab, A.A.: J. Magn. Magn. Mater. **324**, 2199 (2012)
- Oumezzine, E., Hcini, S., Hlil, E.K., Dhahri, E., Oumezzine, M.: J. Alloys Compd. **615**, 553 (2014)
- Khot, V.M., Salunkhe, A.B., Phadatar, M.R., Pawar, S.H.: Chem. Phys. **132**, 782 (2012)
- Rahaman, M.D., Mia, M.D., Khan, M.N.I., Hossain, A.K.M.A.: J. Magn. Magn. Mater. **404**, 238 (2016)
- Zaki, H.M., Dawoud, H.A.: Physica B. **405**, 4476 (2010)
- Shaikh, P.A., Kambale, R.C., Rao, A.V., Kolekar, Y.D.: J. Alloys Compd. **492**, 590 (2010)
- Sabri, K., Rais, A., Taibi, K., Moreau, M., Ouddane, B., Addou, A.: Physica B. **501**, 38 (2016)
- Ahmed, Y.M.Z.: Ceram. Int. **36**, 969 (2010)
- Waje, S.B., Hashim, M., Ismail, I.: J. Magn. Magn. Mater. **323**, 1433 (2011)
- Ortega, N., Kumar, A., Bhattacharya, P., Majumder, S.B., Katiyar, R.S.: Phys. Rev. B. **77**, 014111 (2008)
- Funke, K.: Prog. Solid State Chem. **22**, 111 (1993)
- Atiq, S., Majeed, M., Ahmad, A., Abbas, S.K., Saleem, M., Riaz, S., Naseem, S.: J. Magn. Magn. Mater. **43**, 2486 (2017)

27. Chakrabarty, S., Pal, M., Dutta, A.: *Mater. Chem. Phys.* **153**, 221 (2015)
28. Maxwell, J.C.: *Electricity and Magnetism*. Oxford University Press, London (1973)
29. Jadhav, P.A., Devan, R.S., Kolekar, Y.D., Chougule, B.K.: *J. Phys. Chem. Solids*. **70**, 396 (2009)
30. Vasoya, N.H., Jha, P.K., Saija, K.G., Dolia, S.N., Zankat, K.B., Modi, K.B.: *J. Electron. Mater.* **45**, 917 (2016)
31. Saha, S., Sinha, T.P.: *Phys. Rev. B*. **65**, 1341 (2005)
32. Padmasree, K.P., Kanchan, D.D., Kulkarni, A.R.: *Solid State Ionics*. **177**, 475 (2006)
33. Bergman, R.: *J. Appl. Phys.* **88**, 1356 (2000)
34. Rao, K.S., Krishna, P.M., Prasad, D.M., Gangadharudu, D.: *J. Mater. Sci.* **42**, 4801 (2007)
35. Sivakumar, N., Narayanasamy, A., Ponpandian, N., Govindaraj, G.: *J. Appl. Phys.* **101**, 084116 (2007)
36. Selmi, A., Hcini, S., Rahmouni, H., Omri, A., Bouazizi, M.L., Dhahri, A.: *J. Phase Transit.* **90**, 942 (2017)
37. Sekulic, D.L., Lazarevic, Z.Z., Sataric, M.V., Jovalekic, C.D., Romcevic, N.Z.: *J. Mater. Sci. Mater. Electron.* **26**, 1291 (2015)
38. Dhaou, M.H., Hcini, S., Mallah, A., Bouazizi, M.L., Jemni, A.: *Appl. Phys. A Mater. Sci. Process.* **123**, 8 (2017)
39. Kotnala, R.K., Dar, M.A., Verma, V., Singh, A.P., Siddiqui, W.A.: *J. Magn. Magn. Mater.* **322**, 3714 (2010)
40. Guo, J., Zhang, H., He, Z., Li, S., Li, Z.: *J. Mater. Sci. Mater. Electron.* **29**, 2491 (2018)
41. Omri, A., Bejar, M., Dhahri, E., Es-Souni, M., Valente, M.A., Graça, M.P.F., Costa, L.C.: *J. Alloy. Compd.* **536**, 173 (2012)
42. Kallel, S., Nasri, A., Kallel, N., Rahmouni, H., Peña, O., Khirouni, K.: *M. Oumezzine Physica B*. **406**, 2172 (2011)
43. Khadhraoui, S., Triki, A., Hcini, S., Zemni, S., Oumezzine, M.: *J. Alloys Compd.* **574**, 290 (2013)
44. Johnson, D.: *ZView: a software program for IES analysis, version 2.8*. Scribner Associates, Inc., Southern Pines (2008)
45. Shinde, S.S., Rajpure, K.Y.: *J. Solid State Chem.* **183**, 2886 (2010)